


ORIGINAL ARTICLE

Controlling the phase of iron oxide nanoparticles fabricated from iron(III) nitrate by liquid flame spray

Miika Sorvali¹  | Markus Nikka¹ | Paxton Juuti¹ | Mari Honkanen² |
Turkka Salminen² | Leo Hyvärinen³ | Jyrki M. Mäkelä¹

¹Aerosol Physics Laboratory, Physics Unit, Faculty of Engineering and Natural Sciences, Tampere University, Tampere, Finland

²Tampere Microscopy Center, Tampere University, Tampere, Finland

³Engineering Materials Science, Materials Science and Environmental Engineering Unit, Faculty of Engineering and Natural Sciences, Tampere University, Tampere, Finland

Correspondence

Miika Sorvali, Aerosol Physics Laboratory, Physics Unit, Faculty of Engineering and Natural Sciences, Tampere University, P.O. Box 692, FI-33014 Tampere, Finland.
Email: miika.sorvali@tuni.fi

Funding information

Tampere University of Technology Graduate School

Abstract

Iron oxide nanoparticles were synthesized in a liquid flame spray process from iron(III) nitrate. The choice of chemicals and all other process parameters affects the crystallographic phase composition and the quality of the material. Adjustment of the solvent composition and the gas flow rates was used to control the phase composition of the produced particles. All samples consisted of pure maghemite ($\gamma\text{-Fe}_2\text{O}_3$) or a mixture of maghemite and hematite ($\alpha\text{-Fe}_2\text{O}_3$). When using pure alcohols as solvents, the maghemite/hematite phase ratio could be adjusted by changing the equivalence ratio that describes the oxidation conditions in the flame zone. A large residual particle mode formed in the size range of ~20-700 nm along with a dominant very fine particle mode (2-8 nm). Both phases seemed to contain large particles. A partial substitution of methanol with carboxylic acids turned the hematite phase into maghemite completely, even though some of particles were possibly not fully crystallized. Residual particles were still present, but their size and number could be decreased by raising the heat of combustion of the precursor solution. 30 vol-% substitution of methanol with 2-ethylhexanoic acid was adequate to mostly erase the large particles.

KEYWORDS

iron/iron compounds, liquid flame spray, nanoparticles, synthesis

1 | INTRODUCTION

Iron oxide particles generally occur in one of the four main crystallographic phases depending on the Fe oxidation state: magnetite (Fe_3O_4), maghemite ($\gamma\text{-Fe}_2\text{O}_3$), hematite ($\alpha\text{-Fe}_2\text{O}_3$), or wüstite (FeO), of which the first three are technologically the most relevant.^{1,2} The majority of the applicable potential of magnetite and maghemite lies with their exceptional magnetic properties, whereas hematite possesses, among other things, promising catalytic properties. Applications utilizing magnetic particles include magnetic resonance imaging,^{3,4} microfluidic systems,^{5,6} magnetorheological fluids,^{7,8} and

biomedicine,^{9,10} while hematite has been used, for example, for lithium-ion batteries,^{11,12} gas sensors,¹³ and catalysis.^{14,15}

Magnetite is magnetically the strongest phase, but also maghemite possesses good magnetic properties and is more stable. In addition to the crystallographic phase, the particle size has a strong influence on both magnetic and catalytic properties. The unique magnetic properties stem from superparamagnetism that emerges in the nanoscale, when an adequately small particle size is achieved. As the particle diameter reaches a critical limit of around 20 nm for magnetite,^{16,17} only one magnetic domain remains in each particle. A strong magnetization can then be rapidly switched

This is an open access article under the terms of the Creative Commons Attribution License, which permits use, distribution and reproduction in any medium, provided the original work is properly cited.

© 2019 The Authors. *International Journal of Ceramic Engineering & Science* published by Wiley Periodicals, Inc. on behalf of American Ceramic Society

on and off with an external magnetic field. This fast magnetization switch is utilized, for instance, in magnetorheological fluids.^{7,8} For hematite, the small size of the particles mainly promotes their catalytic activity through an increase in surface area-to-volume ratio. Also, many other properties, such as particle shape, conductivity, and charge injection efficiency, affect the catalytic performance of different catalysts.¹⁴ Therefore, it is important to discover more efficient, economic and environmental friendly ways of producing ultrafine iron oxide nanoparticles of different phases.

Iron oxide powders have been produced with a myriad of fabrication methods and they often consist of a mixture of phases. Chemical methods, such as co-precipitation¹⁸ and hydrothermal synthesis,¹⁹ generally provide good control over the particle properties but usually a noncontinuous, batch-type process, which complicates fast and large-scale production. Gaseous precursors have been used in chemical vapor synthesis of controlled oxidation of iron nanoparticles.²⁰ Physical methods like spray pyrolysis and especially flame synthesis^{21–23} enable much higher production rates, but usually at the expense of process control. As large volumes are often required in industry, the physical methods provide a better basis for upscaling and often an adequate control over the end product. With high volumes, also the price of the precursor becomes extremely important. Therefore, fast and upscalable fabrication methods that can utilize inexpensive liquid precursors are economically excellent alternatives. One flame synthesis method that checks many of these boxes and can be used for producing metal and metal oxide nanoparticles is liquid flame spray (LFS).^{24,25}

Iron nitrate is an inexpensive and abundant precursor that easily dissolves in cheap and common solvents, which makes it an extremely good alternative for large-scale production.²⁶ However, as for most nitrate precursors, effective and complete combustion is quite difficult to achieve, which often leads to a residual mode consisting of large particles. Strobel and Pratsinis²¹ produced maghemite, magnetite, and wüstite by Flame Spray Pyrolysis (FSP). The latter two were only produced in an enclosed chamber by restricting the amount of oxygen in the flame zone, and an open flame only led to maghemite phase. However, hematite has proven to be challenging to produce with flame synthesis methods. Buyukhatipoglu and Clyne²⁷ were able to produce a mixture of maghemite and hematite in a flame synthesis by using an argon stream to deliver iron pentacarbonyl vapor into the flame zone. Finding new solutions to push the complete phase composition toward a single phase would be beneficial.

In this study, we investigated how the phase composition of LFS-made iron oxide nanoparticles can be controlled by adjusting the gas flows and changing the solvent composition. A lot of literature is available on how different parameters, like dispersing gas flow, precursor concentration and

feed rate, and the solvent properties, affect the synthesis conditions.^{28–32} Due to the plethora of parameters affecting the end product, we focused specifically on iron nitrate as the precursor. We found no similar earlier studies that aim to control the hematite/maghemite ratio of flame-synthesized iron oxide particles. Better tunability of the phase increases the versatility of the flame process in utilizing cost-effective nitrate-based precursors. Because the detailed physical and chemical processes happening in the flame are still relatively unclear, studies like these can help achieve understanding of the fundamental processes.

The chemistry of the precursor solution and the flame conditions can be tuned to achieve a more oxidizing or a more reducing environment for particle production, leading to varying phase compositions.^{21,22} One measure that takes into consideration the interplay between many different parameters, and has been used in earlier studies to evaluate the oxidation conditions during FSP synthesis, is the so-called equivalence ratio.^{21,33,34} It considers the amount of oxygen that is necessary for burning all the fuel present in the process (stoichiometric amounts) relative to the actual amount of oxygen present and is defined as:

$$\Phi = \frac{\left(\frac{n_{fuel}}{n_{oxygen}}\right)_{actual}}{\left(\frac{n_{fuel}}{n_{oxygen}}\right)_{stoich}}, \quad (1)$$

where n_{fuel} is the combined amount of substance from the hydrogen flow and the solvent of the precursor solution per unit time, and n_{oxygen} is the amount of substance of oxygen molecules coming from the oxygen flow per unit time.

2 | EXPERIMENTAL

2.1 | Materials

The precursor used for all samples was iron(III) nitrate nonahydrate ($\text{Fe}(\text{NO}_3)_3 \cdot 9\text{H}_2\text{O}$, 98+% (metals basis), Alfa Aesar). The solvents used were methanol (MeOH) (EMSURE[®] ACS, Reag. Ph Eur, Merck), ethanol (EtOH) (99.5+%, Altia Oyj), isopropanol (IPA) (99.8+%, VWR International), 2-ethylhexanoic acid (EHA) (99%, Acros Organics), butanoic acid (ButA) (99%, Merck), and propanoic acid (PropA) (99.5+%, Honeywell Fluka).

Different alcohols were chosen to test the effect of combustion enthalpy on the final product, as the solvents are chemically fairly similar. The three solvents have notable differences in their heat of combustion (HOC): 726 kJ/mol for MeOH, 1367 kJ/mol for EtOH, and 2005 kJ/mol for IPA. If we consider the HOC per unit volume, the percentual differences between the alcohols narrow down: 17.92 kJ/mL for MeOH, 23.45 kJ/mL for EtOH, and 26.2 kJ/mL for IPA, but still clearly differ from each other.

Sample	Solvent composition	H ₂ flow rate (L/min)	O ₂ flow rate (L/min)	Liquid feed rate (mL/min)	Φ
I1	IPA	60	20	4	1.76
I2	IPA	60	20	2	1.63
I3	IPA	30	30	2	0.39
I4	IPA	20	35	2	0.36
I5	IPA	20	35	1	0.32
E1	EtOH	60	20	4	1.73
E2	EtOH	60	20	2	1.61
E3	EtOH	30	30	2	0.58
E4	EtOH	20	35	2	0.35
E5	EtOH	20	35	1	0.32
M1	MeOH	33	15	2	1.21
M2	MeOH	20	35	2	0.33
ME1	MeOH + EHA (95/5 vol-%)	20	35	2	0.33
ME2	MeOH + EHA (85/15 vol-%)	20	35	2	0.34
ME3	MeOH + EHA (70/30 vol-%)	20	35	2	0.34
ME4	MeOH + EHA (50/50 vol-%)	20	35	2	0.35
MB	MeOH + ButA (50/50 vol-%)	20	35	2	0.34
MP	MeOH + PropA (50/50 vol-%)	20	35	2	0.34

TABLE 1 The parameters of different samples. Oxygen was used as the atomizing gas in all cases

2.2 | Nanoparticle synthesis

Iron oxide powders were synthesized by LFS, described in more detail elsewhere.^{28,35} In short, an oxygen or a hydrogen gas flow is used to atomize a liquid precursor solution feed into a turbulent H₂/O₂ flame, where the droplets consequently burn. In contrast to the majority of earlier LFS studies describing nanoparticle synthesis, we used the oxygen flow for atomization in this study, as oxygen seemed to be more effective. The two gas flows emerge from two concentric annular orifices, so they can be easily switched, if desired. The H₂ and O₂ gas flow rates were varied between 20–60 L/minutes and 12–35 L/minutes, respectively. The precursor concentration was kept constant for all cases, so that all precursor solutions contained 40 mg/mL of Fe atoms, which translates to a molar concentration of 0.72 mol/L. Also, the liquid feed rate was mostly kept constant at 2 mL/minutes, which results in Fe atom flow of 80 mg/minutes through the flame, but a few exceptions were chosen in order to see if the liquid feed rate has a profound effect on the phase ratio. All different samples are presented in Table 1 along with their equivalence ratios.

The powder samples were collected with an electrostatic precipitator that consisted of two nearly parallel metal plates, one of which had thin metal wires attached to it. The metal wires worked as corona needles when a high voltage (20–35 kV) was applied to the plate. The other plate was

grounded, creating a strong electric field between them. The flame was directed between the plates, so that the nanoparticle flux moved through the electric field. The particles experienced electrical charging from the corona discharges present around the tip of the metal wires and a consequent deposition onto the grounded plate. The deposited particles were carefully scraped off the metal plate and collected in a container for analysis.

2.3 | Characterization and sample preparation

The crystal structure of the powders was characterized with X-ray powder diffraction (XRD) (Panalytical Empyrean, monochromatized CuK_α radiation 15° < 2θ < 70°). The recorded XRD patterns were analyzed by Rietveld refinement, using BRASS 2 program.³⁶ The structure models used for the refinement were acquired from American Mineralogist Crystal Structure Database (AMCSD) with the codes 0020585 for maghemite (space group Fd-3m) and 0000143 for hematite (space group R-3c). Since several models with different space groups were available for maghemite, the model used was chosen based on which gave the best fit for pure maghemite samples. Further structural information was obtained with a Raman microscope (Renishaw inVia™ Qontor®) that enabled simultaneous optical microscopy and the recording of Raman spectra from specifically chosen

locations. The wavelength used for excitation was 532 nm. The Raman samples were prepared by attaching a piece of double-sided tape on a microscope slide and spreading a small amount of a collected powder onto it. The powder samples were thick enough to eliminate any signal emanating from the substrate. With iron oxide nanoparticles, one must be very careful with the laser power, because magnetite and maghemite are easily turned into other phases, if the intensity of the laser beam is too high.^{37,38} Therefore, a very low laser power (~0.3 mW) was chosen to prevent phase changes during the measurements.

The sizes and shapes of the particles were analyzed with a transmission electron microscope (TEM) (JEOL JEM-F200). The TEM samples were prepared by dispersing powders in ethanol, followed by 15-minutes ultrasonic bath to break large agglomerates, and finally dipping a TEM grid with a carbon film in the dispersion. As the ethanol evaporated, the particles attached to the TEM grid sufficiently well. TEM imaging is a reliable way to analyze the precise size of the primary particles, but a TEM sample is always a very small representation of the whole powder, so we used the XRD results to interpret the whole picture. Due to various error sources and possible polydispersity, the XRD results cannot be directly translated into the actual size of the particles, but rather to indicate the presence of large particles, when combined with TEM studies. The average crystallite sizes can be obtained from Rietveld analyses.

3 | RESULTS AND DISCUSSION

3.1 | Pure alcohols as solvents

XRD works well in distinguishing hematite from maghemite and magnetite, since there are several significant peaks without overlap. Two of these distinct reflections are at 2θ angles of a little above 30° for maghemite/magnetite and 33° for hematite. Figure 1 shows these two peaks for three samples produced with EtOH as the solvent with varying gas flows. All of the patterns were scaled based on the 30° peak to demonstrate the change in the ratio between the peak areas as the ratio of the gas flows shifts.

When there is more oxygen available in the flame zone, a larger portion of the produced particles formed in the more oxidized hematite phase. Li et al¹⁶ has stated that flame-made iron oxide generally crystallizes as maghemite, and we did not come across any studies where hematite powder would have been fabricated directly in liquid-fed FSP.

We used Rietveld refinement to quantify the weight percentages of each phase in each sample from the XRD results. The Rietveld plots for all samples and some chosen parameters are presented in Figures S1-S6 and Table S1. As the hematite phase was difficult to fully refine in samples with low hematite fractions, there is more uncertainty for these. Because the following Raman results indicated that the

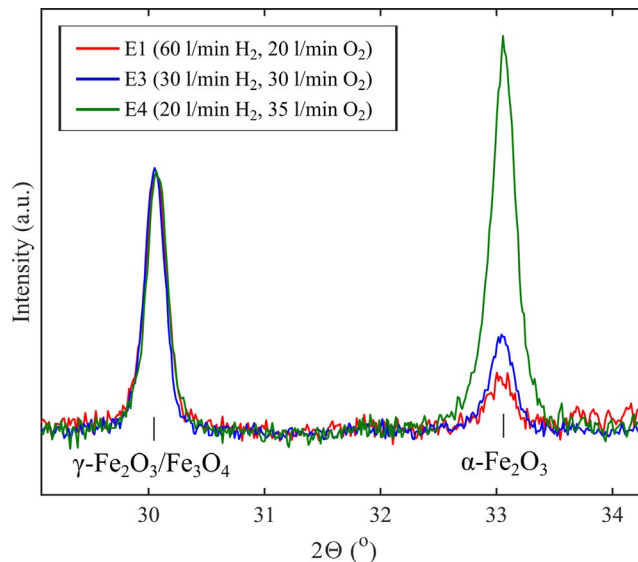


FIGURE 1 Patterns of two XRD reflections for samples produced with ethanol as the solvent and varying gas flows. All intensities were normalized based on the 30° peak

samples consisted of only maghemite and hematite, we will not be mentioning magnetite from now on. By trying to figure out the correlation of different parameters to the phase composition, it turned out that the equivalence ratio (Φ) could be used to describe the phase behavior quite well. The iron nitrate precursor is not considered in the calculations, since it is assumed to go through an endothermic decomposition reaction.³⁹ Because we used an atmospheric synthesis process, the theoretical amount of oxygen is most likely not the actual amount present due to possible oxygen diffusion from the surrounding air. Figure 2 depicts the calculated maghemite fraction as a function of equivalence ratio.

All of the samples with an alcohol as the solvent fall quite nicely on a curve, but there seems to be some effect, possibly originating from the differing chemistry of the solvents, that places most IPA samples above the EtOH samples. The effect of chain branching and carbon chain length could be studied by experimenting with different alcohols. In general, the HOC values do not seem to have a significant effect on the phase behavior. It looks like the maghemite fraction saturates at around $\Phi = 1$, which could be a result of oxygen diffusion from the surrounding atmosphere. As the oxygen flow in the flame decreases, the amount of diffused oxygen from the surroundings increases. Therefore, the real equivalence ratio probably cannot be raised much above 1 in an open flame setup. In contrast, the low end of the curve seems very sensitive to changes in the equivalence ratio. With the synthesis setup used, it was difficult to obtain a stable flame with lower Φ values, so we did not go any lower. However, experimenting with even lower equivalence ratios offers an interesting path for future work with experimental setup modification. It would be interesting to see how far down this curve can

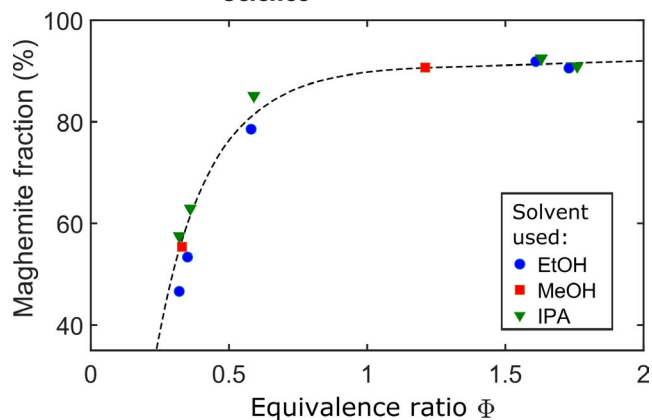


FIGURE 2 The weight percentage of maghemite as a function of equivalence ratio in samples synthesized using different alcohols as the solvent. The rest of the samples consisted of hematite phase

predict the phase composition. Based on these results, EtOH might be the best of these three alternatives for a solvent, when trying to reach higher hematite fractions.

Even though preceding literature indicates that open flame samples should contain maghemite but no magnetite, we wanted to confirm this with Raman microscopy. Figure 3 shows the optical microscope images along with the recorded Raman spectra from the indicated locations for three samples with different gas flows. The calculated weight percentages from Rietveld refinement for each phase are presented above the micrographs for the corresponding samples. Also, typical spectra for hematite and maghemite along with characteristic features are marked.

The measurements of all samples basically only gave two kinds of spectra, or some combination of these, that can be identified as maghemite and hematite, based on the literature.^{37,38,40} None of the measurements gave a pattern that would clearly resemble that of magnetite, so we concluded that the powders comprise only maghemite and hematite. The hematite patterns show clearly the typical two A_{1g} modes (226 and 500 cm^{-1}) and the five E_g modes (245, 293, 298, 413 and 612 cm^{-1}).⁴¹ The peaks at 293 and 298 cm^{-1} are overlapping a bit, but they can be distinguished based on the shape of the peak. In addition to these, there is a residual peak at around 660 cm^{-1} , which is often seen in hematite samples.³⁷ According to Zoppi et al.,⁴² it might originate from the lack of long-range order or an impurity phase. The intense peak at 1320 cm^{-1} comes from a two-magnon scattering arising from hematite's antiferromagnetic nature.³⁸

Maghemite can be identified by four broad bands at around 350, 500, 700, and 1440 cm^{-1} .^{38,43} However, for maghemite the locations of the peaks are not as well determined as for hematite. This might be due to the seeming uncertainty considering the exact structure of maghemite, as multiple possible structure models have been reported in the literature.⁴⁴⁻⁴⁶ Nevertheless, the recorded patterns fit many reported patterns well. The three

main peaks used for the identification refer to Raman active phonon modes T_{2g} (365 cm^{-1}), E_g (511 cm^{-1}), and A_{1g} (700 cm^{-1}).⁴⁷

The optical micrographs of samples with low hematite fractions gave mostly brown/green background with small yellowish dots here and there. If the spectrum from anywhere in the dominant background was recorded, it indicated the maghemite phase, and if the laser was pointed to a yellow spot, either a hematite pattern or a sum of hematite and maghemite was recorded. This phenomenon was observed for all samples, and some additional images and patterns are presented in Figure S7. For some samples with fairly low hematite fractions, the hematite particles seemed to agglomerate together, forming large yellow areas. This could be due to differences in magnetic or electric properties between the particles of different phases. When the hematite fraction grew, the amount of the yellow area in the images increased and the phases blended together more, leading to more mixed phase Raman patterns. The Rietveld refinement and the Raman microscopy results support each other very well. The ratio of the yellow area with respect to brown/green gives a good indication of the actual phase composition. Since Raman microscopy requires very little sample preparation and the measurements are fast to perform, it could possibly be used as a quick, qualitative technique to give an idea of the phase composition of iron oxide samples. We did not come across any literature referring to similar optical phase characterization.

In addition to the phase composition, we were interested in the size distribution of the particles, since the primary particle size is an important factor considering the functionality of various applications. Figure 4 shows TEM images of some samples with different parameters and the primary particle size as a function of equivalence ratio.

The top row in Figure 4A represents the overwhelming majority of the TEM sample areas. Mostly the powders were composed of a very fine particle mode in the size range of 2-8 nm, depending on the process parameters. The estimated mean primary particle size, d_{TEM} , for the dominant fine mode was calculated from TEM images for those samples that were imaged. The size distributions for this dominant mode looked very narrow for all samples, most of the particles falling inside $\pm 1-2$ nm from the average. If we consider the size of primary particles in different flame conditions, one of the most important factors is the residence time of the particles in the flame. One of the best single indicators for the residence time is the length of the flame, which determines the size of the high-temperature zone. Madler et al.³¹ showed a linear dependence between the equivalence ratio and the flame height. This effect can be seen in Figure 4B. Even though the equivalence ratio is not the only factor affecting the residence time, the estimated average size of the dominant mode seems to follow it rather linearly. This indicates that the amount of evaporated precursor, and therefore residual particles, is probably reasonably similar in all samples. A significant decrease in the

residual mode would most likely tilt the correlation. Based on the average crystallite sizes, simply raising the equivalence ratio has little effect on the formation of the residual mode, but it rather mostly affects the size of the fine mode and the phase composition. We tried to briefly with four samples, I1, I5, E1, and E5, see if halving or doubling the liquid feed rate has a large impact on the phase ratio and residual particles. Since no clear differences were visible in the XRD data, liquid-to-gas ratio is most likely not a very important factor in this regard.

The bottom row in Figure 4A represents the very few areas present on the TEM samples that revealed collections of significantly larger particles that had a very wide size distribution ranging from tens of nanometers to several hundred nanometers. This mode is presumed to be a so-called residual mode that has formed from precursor solution droplets that did not evaporate after atomization, whereas the fine mode has most likely nucleated from gas phase after complete evaporation.^{25,32} We could not find these large particles in every sample, so we used the average crystallite sizes obtained from Rietveld refinement to indicate the presence of residual particles. Since some of these particles are two orders of magnitude larger than most, even a small amount of them gives a significant contribution to the measured XRD patterns. These particles seemed to be mostly single crystals, but the TEM images were not adequate to tell for certain. The average crystallite sizes obtained from Rietveld refinement ranged a lot between 27.3 and 515.0 nm (Table S1), varying between the two phases. It does not give a reliable measure for the particle size, but strongly indicates the presence of residual particles in all samples. Also, the phases do not seem to have large enough difference in total for the residual mode to only consist of maghemite or hematite. Most likely, both phases have a mixed composition. This indicates that the phase of a particle is not directly dependent on the formation path, when considering gas-to-particle versus droplet-to-particle routes.

One of the possible ways for the formation of residual particles is hydrolysis in the liquid phase.³⁷ The precursor itself contains crystal water, but much more water vapor forms in the H_2/O_2 flame. Since alcohols are generally soluble with water, this could allow condensation of water vapor and dissolution to the droplets. However, hydrolysis of iron nitrate should lead to hematite.^{37,48} Because it seems that hematite is present in both phases, this is likely not the only mechanism involved. Condensating water can also hinder the combustion of the solution droplets, leading to incomplete combustion.⁴⁹ A challenge for future studies is removing the residual mode while maintaining the phase control.

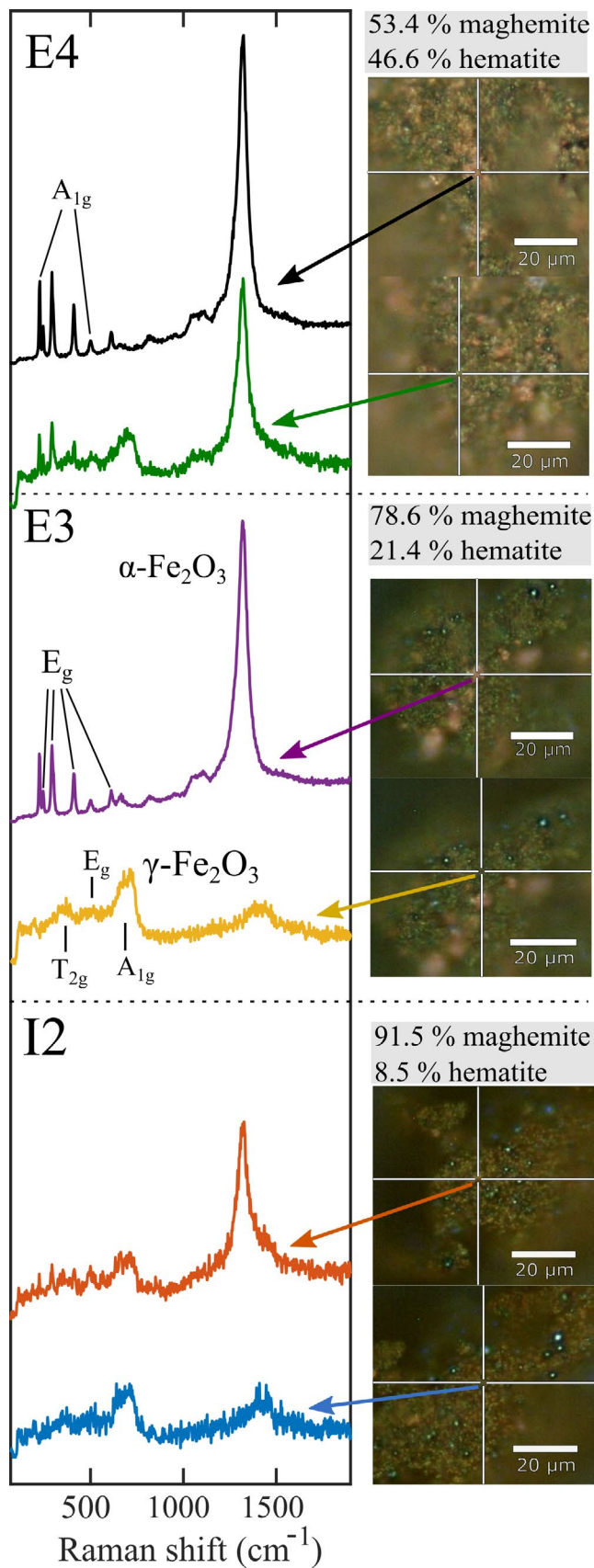
3.2 | Mixtures of alcohols and carboxylic acids

We wanted to study the effect of carboxylic acids in the solvent on the phase composition of the produced powder.

It was hypothesized earlier that the hematite portion of the particles could come from the residual mode. The results presented above, however, contradict this assumption. EHA has been used before to eliminate residual particles in flame synthesis.^{26,50} Rosebrock et al^{49,51} found in single droplet experiments that in some cases the addition of EHA to the precursor solution led to strong droplet explosions, which led to smaller particles. We wanted to see the effects of three carboxylic acids with differing chain lengths. 50% of the MeOH volume in the precursor solution was substituted with an equal volume of PropA, ButA, and EHA. Also, the effect of the amount of EHA was studied by making 5, 15, and 30% substitutions in addition to the 50% samples. For most of the samples, only one set of gas flows, namely 20 L/minutes of H_2 and 35 L/minutes of O_2 , was chosen to emphasize the role of the solvent, because a shift in the direction of either phase would become most visible. Surprisingly, the addition of carboxylic acids erased the hematite phase completely in all cases, even though the equivalence ratios were very low (0.33-0.35). Figure 5A compares the XRD patterns of three samples with identical gas flows, but different solvent compositions. The pattern of M2 was slightly scaled down to fit the intensities of the other samples better. Therefore, Figure 5A does not represent the amounts of phases between the samples.

The powders that had 5 vol-% of EHA and 50 vol-% of PropA gave almost identical XRD patterns with strong reflections, and all of the hematite peaks vanished compared with the pure MeOH sample. When at least 15 vol-% of EHA was added to the solution, the XRD peaks got broader and weaker (Figures S5 and S6). Also, a larger background was measured for these samples. This refers to smaller particle sizes, but also to the possible presence of amorphous material and carbonaceous residua. The low intensities with a high background made Rietveld refinement quite difficult, and the average crystal sizes cannot be regarded very reliable. This, however, indicates a lower amount of large particles.

The purity of the phase was also characterized by Raman microscopy, and the results from the alcohol samples can be used to analyze the acquired data. Figure 5B presents two Raman micrographs and the recorded spectra from the marked locations. All of the recorded patterns from carboxylic acid samples gave only maghemite patterns and all microscope images showed the absence of the yellow areas indicating hematite. At some spots, very weak spectra without clear peaks were recorded, which in part indicates incomplete crystallization (Figure S8). Since our emphasis was on phase control, we did not try different gas flows, but increasing the equivalence ratio could lead to a higher degree of crystallization through longer residence times and higher temperatures.



Just like for the alcohol samples, TEM imaging was used to characterize the primary particle size. Figure 6 shows TEM images of various samples produced with

FIGURE 3 Optical micrographs of three different alcohol samples (E4, E3 and I2) and the recorded Raman spectra from the indicated locations. The corresponding phase compositions obtained by Rietveld analysis are presented above the micrographs. Typical hematite and maghemite patterns and the characteristic peaks are also marked

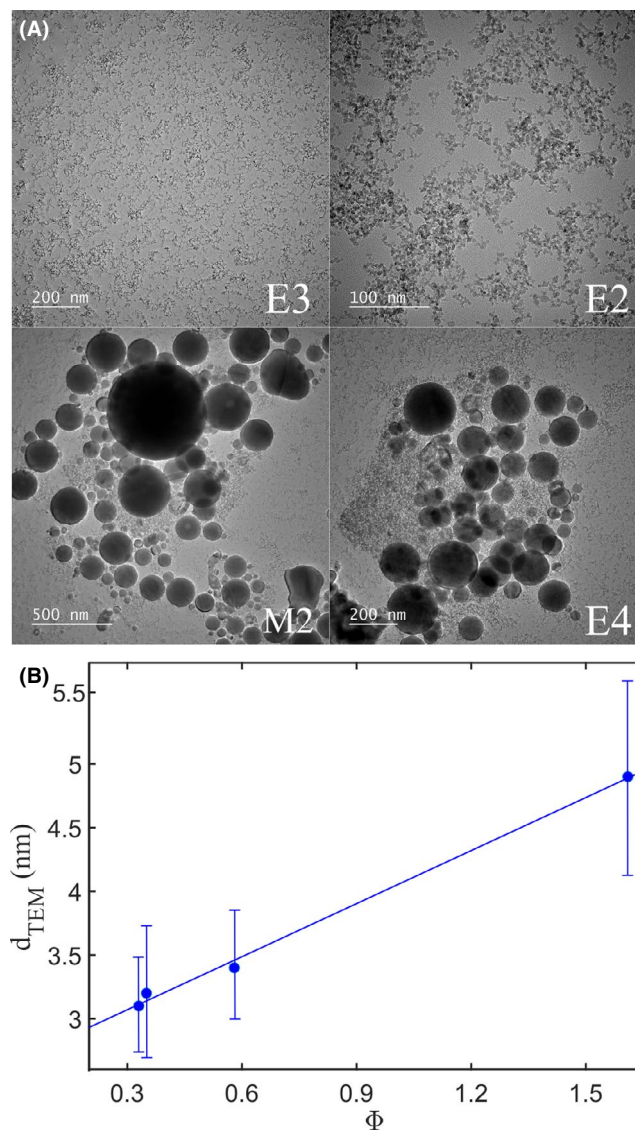


FIGURE 4 A, TEM images of some samples (E2, E3, E4 and M2) produced with pure alcohols as solvents and B, the average primary particle size as a function of equivalence ratio. The standard deviations are marked with error bars. In (A), the top row represents the majority of the sample areas and the bottom row the very few areas with larger particles

different amounts of EHA in the precursor solution. In accordance to Figure 4, the top row shows the dominant phase of the TEM sample areas, whereas the bottom row represents the very few areas with larger particles. These are the largest collections of residual particles that were

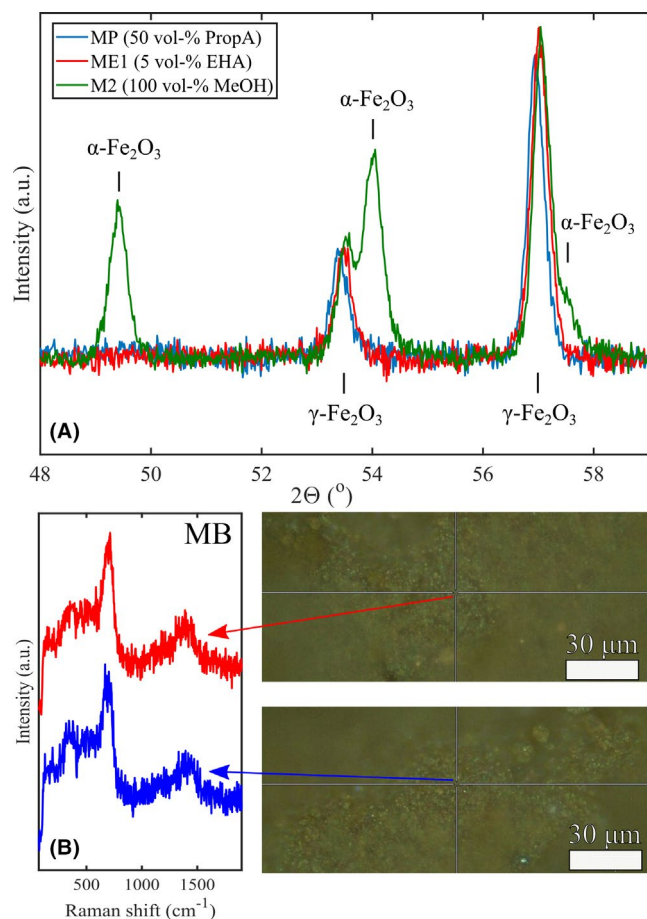


FIGURE 5 A, Patterns of three XRD reflections of a MeOH sample (M2) and two samples with identical gas flows, but carboxylic acids added to the solvent mixture (MP and ME1), and B, optical micrographs with recorded Raman spectra from the sample with butanoic acid. The pattern of M2 was slightly scaled down to fit the intensities of the other samples to better emphasize the disappearance of the hematite peaks

found in the samples in question. As the amount of EHA in the precursor solution increased, the primary particle size in the fine mode also increased. Simultaneously, the amount and the size of the residual particles decreased. These two processes counteracting each other makes sense, because the elimination of the residual mode increases the amount of evaporated precursor in the flame, which then leads to enhanced condensation and growing particle size. Figure 7 shows the d_{TEM} values calculated from the TEM images values as a function of HOC of the corresponding precursor solution, which turned out to be a better indicator than Φ in this case.

The blue dots in Figure 7, referring to EHA samples, fall quite well on a straight line, but the one data point with propanoic acid seems to be an outlier. This is presumably caused by the different chemistry between the two carboxylic acids. Now, the equivalence ratio does not change much and the increase in the primary particle size stems from the elimination

of residual particles. Based on TEM images, the 50 vol-% substitution with the two shorter-chained carboxylic acids still led to formation of a significant amount of larger particles, as with alcohol samples. The same thing also happened with 5 vol-% substitution with EHA, but as the fraction of EHA in the solvent mixture was raised, less residual particles were found, and at 30 vol-% they seemed to be mostly gone. As was mentioned before, the average crystallite sizes are not reliable due to poor refinement, but the significantly lower values for the samples with 15, 30, and 50 vol-% of EHA in the precursor solution compared to others (12.7, 8.6, and 11.5 nm, respectively) indicate a lower amount of large particles. The mechanism of residual reduction behind the increasing addition of EHA could be studied by testing if the same effect can be achieved by adjusting the gas flows for solutions with lower EHA content.

Strobel and Pratsinis²⁶ produced homogeneous nanoparticles from metal nitrates by adding carboxylic acids to the solution, but our results indicate that this does not always lead to the elimination of the residual mode, but it rather turns the hematite phase into maghemite. The reason for this is still uncertain. They suggested that nitrates could be converted into carboxylates at elevated temperatures in the presence of carboxylic acids. Also, Chiarello et al⁵² stated that fast heating would lead to the formation of metal complexes when using metal nitrates. It is possible that carboxylic acids turn the iron nitrate into a metal complex that has no formation route to hematite in flame conditions, even with high oxygen concentrations. We did not find studies that would confirm this in FSP synthesis, though. There is research regarding chemical synthesis of iron oxide nanoparticles that introduce various chemicals to turn iron nitrate into other intermediate precursors. Habibi and Kiani⁵³ turned iron nitrate into iron(III) citrate by reacting it with citric acid, iron(III) acetate by reacting it with ammonium acetate and iron(III) oxalate by reacting it with oxalic acid. This kind of reactions, if fast enough, could happen in the flame, and lead to various reaction routes into the final product.

Meierhofer et al⁵⁴ produced $\text{Li}_4\text{Ti}_5\text{O}_{12}$ particles from different precursor/solvent combinations. The highest quality particles were obtained from solutions containing EHA. They stated that for titanium isopropoxide, EHA could prevent hydrolysis/condensation reactions. If hydrolysis is the reason for the presence of hematite phase, similar effect with iron nitrate could explain this. They also observed in single droplet experiments that addition of EHA led to earlier microexplosions of precursor solution droplets promoted the release of the precursors into the gas phase. These two effect could at least in part be responsible for the decrease in residual particle size and number.

Grigorie et al⁵⁵ produced hematite and maghemite from iron(III) nitrate by thermal decomposition. They mixed the precursor with various amounts of polyethylene glycol

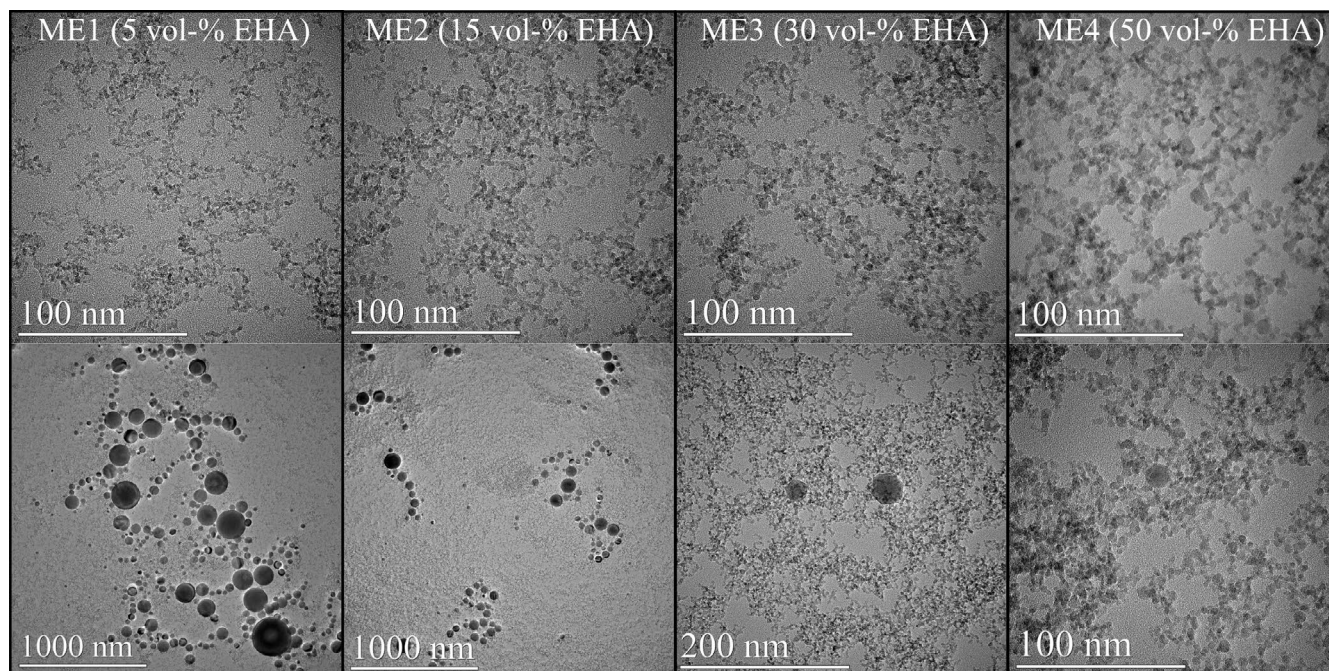


FIGURE 6 TEM images of samples with different volume fractions of MeOH substituted with EHA. The top row represents the majority of the sample areas, whereas the bottom row shows the largest collection of residual particles found on the samples

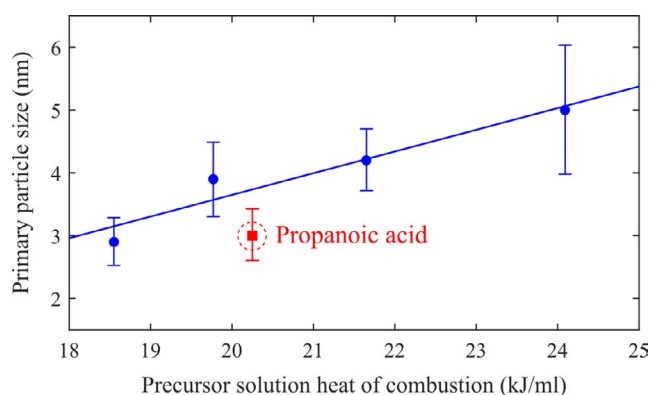


FIGURE 7 The average primary particle sizes calculated from TEM images for carboxylic acid-containing samples as a function of the heat of combustion for the precursor solution. The blue dots refer to samples containing increasing amount of EHA and the red square contained 50 vol-% propanoic acid. The standard deviations are marked with error bars

(PEG), which worked as a reducing agent. With low PEG concentration, mostly hematite was formed, but as the concentration was raised adequately, it turned into maghemite. Perhaps carboxylic acids provide a similar reducing environment in the flame. The conclusions from chemical syntheses in much lower temperatures and longer times are not directly applicable to LFS conditions, but they could give a hint of the actual mechanisms. This should be tested by adding other reducing agents to the precursor solution instead of carboxylic

acids. If this is the reason for the elimination of the hematite phase, addition of oxidizing agents to the solution could potentially increase the hematite fraction. The incompatibility of strong oxidizers with flammable solvents presents a challenge, however.

These results support further the claim that the residual mode and the hematite phase are not directly linked to each other, as clearly bimodal particle size distributions were found for MP, MB, ME1, ME2, and all of the alcohol samples. It would be interesting to see if using an alcohol with higher heat of combustion mixed with carboxylic acids could be used for eliminating the residual mode with a lower carboxylic acid content. According to Jossen et al.³², a large ratio of solvent boiling point to precursor melting point would also promote the production of homogeneous particles. This would partly explain the differences between PropA, ButA, and EHA, as their boiling points are 141.5, 163.8, and 288.1°C, respectively, compared with that of MeOH (64.7°C).

4 | CONCLUSIONS

Iron oxide particles can form in various different crystallographic phases. We investigated how the phase of iron oxide nanoparticles can be controlled in liquid flame spray synthesis when using iron(III) nitrate as the precursor. We succeeded in finding process parameters to intentionally adjust the hematite/maghemite ratio of flame-synthesized iron oxide nanoparticles

in a systematic way. We are not aware of earlier studies where the hematite/maghemite ratio has been tuned in a flame-based method. Therefore, we believe that these results will increase the potential of cost-effective nitrate precursors for generating highly dispersed iron oxide nanomaterials.

The solvent composition and the oxygen and hydrogen gas flow rates were the main parameters studied. All collected powder samples were found to consist of either maghemite or a mixture of maghemite and hematite phases, along with possible amorphous material. In nanoparticle synthesis from a liquid precursor, unwanted larger residual particles can form as a result of incomplete evaporation. We were also interested in the influence of residual particles in the phase composition.

When different pure alcohols (methanol, ethanol, or isopropanol) were used as solvents, equivalence ratio that describes the amount of oxygen in the flame zone was found to have a strong correlation with the phase ratio. Oxygen-rich conditions pushed the ratio toward hematite, whereas oxygen-lean conditions promoted maghemite formation, but always having both phases present. Even though most of the particles were very small (2–8 nm), all alcohol samples contained a residual mode that consisted of significantly larger particles (up to several hundred nanometers). Both particle modes seemed to consist of a mixture of the two phases. The equivalence ratio affected the primary particle size of the dominant fine mode in addition to the phase composition.

Mixing carboxylic acids (propionic acid, butanoic acid, or 2-ethylhexanoic acid) with methanol in the solvent mixture led to the complete elimination of the hematite phase, which indicates that the effect of equivalence ratio to the phase composition is tightly linked to the chemical composition of the precursor solution. This happened possibly due to a carboxylic acid-induced conversion of iron nitrate to an intermediate metal complex that has no formation path into hematite in the flame conditions, but this could not be confirmed. When using the two shorter-chained carboxylic acids with low heat of combustion or a small amount of 2-ethylhexanoic acid, a significant amount of residual particles formed. The size and the number of residual particles could, however, be changed by adjusting the mixing ratio of methanol and 2-ethylhexanoic acid, but simultaneously leaving possibly amorphous material. As the amount of 2-ethylhexanoic acid increased in the solvent mixture, simultaneously raising its heat of combustion, the residual mode shrunk. The more complete evaporation of the precursor solution led to an increase in the primary particle size.

The interplay of all different parameters and the precursor solution chemistry is not yet fully understood. More research is needed to understand the impact of different parameters in controlling the phase of iron oxide particles in FSP synthesis, while simultaneously ensuring their homogeneity.

ACKNOWLEDGMENTS

M. Sorvali and P. Juuti want to acknowledge the TUT graduate school for financial support. This work made use of Tampere Microscopy Center facilities at Tampere University.

ORCID

Miika Sorvali  <https://orcid.org/0000-0003-2697-4922>

REFERENCES

1. Wu W, He Q, Jiang C. Magnetic iron oxide nanoparticles: synthesis and surface functionalization strategies. *Nanoscale Res Lett.* 2008;3:397–415.
2. Teja AS, Koh P-Y. Synthesis, properties, and applications of magnetic iron oxide particles. *Prog Cryst Growth Ch.* 2009;55:22–45.
3. Laurent S, Forge D, Port M, Roch A, Robic C, Elst LV, et al. Magnetic iron oxide nanoparticles: synthesis, stabilization, vectorization, physicochemical characterizations, and biological applications. *Chem Rev.* 2008;108:2064–110.
4. Nosrati H, Salehiabar M, Fridoni M, Abdollahifar M-A, Manjili HK, Davaran S, et al. New insight about biocompatibility and biodegradability of iron oxide magnetic nanoparticles: stereological and in vivo MRI monitor. *Sci Rep.* 2019;9:7173.
5. Gijs MAM, Lacharme F, Lehmann U. Microfluidic applications of magnetic particles for biological analysis and catalysis. *Chem Rev.* 2010;110:1518–63.
6. Hsu M-C, Alfadhel A, Forouzandeh F, Borkholder DA. Biocompatible magnetic nanocomposite microcapsules as microfluidic one-way diffusion blocking valves with ultra-low opening pressure. *Mater Des.* 2018;150:86–93.
7. Jönkkäri I, Sorvali M, Huhtinen H, Sarlin E, Salminen T, Haapanen J, et al. Characterization of bidisperse magnetorheological fluids utilizing maghemite ($\gamma\text{-Fe}_2\text{O}_3$) nanoparticles by flame spray pyrolysis. *Smart Mater Struct.* 2017;26(6):095004.
8. Kciuk M, Turczyn R. Properties and application of magnetorheological fluids. *JAMME.* 2006;18(1–2):127–30.
9. Gupta AK, Gupta M. Synthesis and surface engineering of iron oxide nanoparticles for biomedical applications. *Biomaterials.* 2005;26:3995–4021.
10. Usov NA. Iron oxide nanoparticles for magnetic hyperthermia. *SPIN.* 2019;9(2):1940001.
11. Zhu J, Lu Y, Chen C, Ge Y, Jasper S, Leary JD, et al. Porous one-dimensional carbon/iron oxide composite for rechargeable lithium-ion batteries with high and stable capacity. *J Alloy Compd.* 2016;672:79–85.
12. Park J, Yoo H, Choi J. 3D ant-nest network of $\alpha\text{-Fe}_2\text{O}_3$ on stainless steel for all-in-one anode for Li-Ion battery. *J Power Sources.* 2019;431:25–30.
13. Aronniemi M, Saino J, Lahtinen J. Characterization and gas-sensing behavior of an iron oxide thin film prepared by atomic layer deposition. *Thin Solid Films.* 2008;516:6110–5.
14. Demirci S, Yurddaskal M, Dikici T, Sarioğlu C. Fabrication and characterization of novel iodine doped hollow mesoporous hematite (Fe_2O_3) particles derived from sol-gel method and their photocatalytic performances. *J Hazard Mater.* 2018;345:27–37.

15. Tamirat AG, Rick J, Dubale AA, Su W-N, Hwang B-J. Using hematite for photoelectrochemical water splitting: a review of current progress and challenges. *Nanoscale Horiz.* 2016;1:243–67.
16. Li D, Teoh WY, Selomulya C, Woodward RC, Amal R, Rosche B. Flame-sprayed superparamagnetic iron oxide and silica-coated maghemite nanoparticles: synthesis, characterization, and protein adsorption-desorption. *Chem Mater.* 2006;18:6403–13.
17. Li Q, Kartikowati CW, Horie S, Ogi T, Iwaki T, Okuyama K. Correlation between particle size/domain structure and magnetic properties of highly crystalline Fe₃O₄ nanoparticles. *Sci Rep.* 2017;7:9894.
18. Jolivet J-P, Chanéac C, Tronc E. Iron oxide chemistry. From molecular clusters to extended solid networks. *Chem Commun.* 2004;10:481–3.
19. Tadić M, Čitaković N, Panjan M, Stojanović Z, Marković D, Spasojević V. Synthesis, morphology, microstructure and magnetic properties of hematite submicron particles. *J Alloys Compd.* 2011;509:7639–44.
20. Ruusunen J, Ihalainen M, Koponen T, Torvela T, Tenho M, Salonen J, et al. Controlled oxidation of iron nanoparticles in chemical vapour synthesis. *J Nanopart Res.* 2014;16:2270.
21. Strobel R, Pratsinis SE. Direct synthesis of maghemite, magnetite and wustite nanoparticles by flame spray pyrolysis. *Adv Powder Technol.* 2009;20:190–4.
22. Kumfer BM, Shinoda K, Jeyadevan B, Kennedy IM. Gas-phase flame synthesis and properties of magnetic iron oxide nanoparticles with reduced oxidation state. *J Aerosol Sci.* 2010;41:256–65.
23. Li Y, Hu Y, Huang G, Li C. Metallic iron nanoparticles: flame synthesis, characterization and magnetic properties. *Particuology.* 2013;11:460–7.
24. Mäkelä JM, Aromaa M, Rostedt A, Krinke TJ, Janka K, Marjamäki M, et al. Liquid flame spray for generating metal and metal oxide nanoparticle test aerosol. *Hum Exp Toxicol.* 2009;28(6–7):421–31.
25. Mäkelä JM, Haapanen J, Harra J, Juuti P, Kujanpää S. Liquid flame spray – a hydrogen-oxygen flame based method for nanoparticle synthesis and functional nanocoatings. *KONA Powder Part J.* 2017;34:141–54.
26. Strobel R, Pratsinis SE. Effect of solvent composition on oxide morphology during flame spray pyrolysis of metal nitrates. *Phys Chem Chem Phys.* 2011;13:9246–52.
27. Buyukhatipoglu K, Clyne AM. Controlled synthesis of α -Fe₂O₃ and Fe₃O₄ nanoparticles: effect of flame configuration, flame temperature, and additive loading.
28. Aromaa M, Keskinen H, Mäkelä JM. The effect of process parameters on the Liquid Flame Spray generated titania nanoparticles. *Biomol Eng.* 2007;24:543–8.
29. Kammler HK, Mädler L, Pratsinis SE. Flame synthesis of nanoparticles. *Chem Eng Technol.* 2001;24(6):583–96.
30. Tikkanen J, Gross KA, Berndt CC, Pitkänen V, Keskinen J, Raghu S, et al. Characteristics of the liquid flame spray process. *Surf Coat Technol.* 1997;90:210–6.
31. Mädler L, Stark WJ, Pratsinis SE. Flame-made ceria nanoparticles. *J Mater Res.* 2002;17(6):1356–62.
32. Jossen R, Pratsinis SE, Stark WJ, Mädler L. Criteria for flame-spray synthesis of hollow, shell-like, or inhomogeneous oxides. *J Am Ceram Soc.* 2005;88(6):1388–93.
33. Mädler L, Kammler HK, Mueller R, Pratsinis SE. Controlled synthesis of nanostructured particles by flame spray pyrolysis. *J Aerosol Sci.* 2002;33:369–89.
34. Aromaa M, Arffman A, Suhonen H, Haapanen J, Keskinen J, Honkanen M, et al. Atmospheric synthesis of superhydrophobic TiO₂ nanoparticle deposits in a single step using Liquid Flame Spray. *J Aerosol Sci.* 2012;52:57–68.
35. Keskinen H, Aromaa M, Heine MC, Mäkelä JM. Size and velocity measurements in sprays and particle producing flame sprays. *Atom Sprays.* 2008;18:1–26.
36. Birkenstock J, Fischer RX, Messner T. BRASS 1.0beta: The Bremen Rietveld Analysis and Structure Suite. *Zentrallabor für Kristallographie und Angewandte Materialwissenschaften, Fachbereich Geowissenschaften, University of Bremen* 2003.
37. Bersani D, Lottici PP, Montenero A. Micro-Raman investigation of iron oxide films and powders produced by sol-gel syntheses. *J Raman Spectrosc.* 1999;30:355–60.
38. De Faria DLA, Silva SV, Oliveira MT. Raman microscopy of some iron oxides and oxyhydroxides. *J Raman Spectrosc.* 1997;28:873–8.
39. Wiczorek-Ciurowa K, Kozak AJ. The thermal decomposition of Fe(NO₃)₃·9H₂O. *J Therm Anal Calorim.* 1999;58:647–51.
40. Hanesh M. Raman spectroscopy of iron oxides and (oxy)hydroxides at low laser power and possible applications in environmental magnetic studies. *Geophys J Int.* 2009;177:941–8.
41. Beattie IR, Gilson TR. The single-crystal Raman spectra of nearly opaque materials. Iron(III) oxide and chromium(III) oxide. *J Chem Soc.* 1970;980–6.
42. Zoppi A, Lofrumento C, Castellucci EM, Migliorini MG. The Raman spectrum of hematite: possible indicator for a compositional firing distinction among terra sigillata wares. *Ann Chim-Rome.* 2005;95:239–46.
43. Ohtsuka T, Kubo K, Sato N. Raman spectroscopy of thin corrosion films on iron at 100 to 150 C in air. *Corrosion.* 1986;42(8):476–81.
44. Pecharrmán C, González-Carreño T, Iglesias JE. The infrared dielectric properties of maghemite, γ -Fe₂O₃ from reflectance measurement on pressed powders. *Phys Chem Miner.* 1995;22(1):21–9.
45. Jørgensen J-E, Mosegaard L, Thomsen LE, Jensen TR, Hanson JC. Formation of γ -Fe₂O₃ nanoparticles and vacancy ordering: an in situ X-ray powder diffraction study. *J Solid State Chem.* 2007;180(1):180–5.
46. Solano E, Frontera C, Puig T, Obradors X, Ricart S, Ros J. Neutron and X-ray diffraction study of ferrite nanocrystals obtained by microwave-assisted growth. A structural comparison with the thermal synthetic route. *J Appl Crystallogr.* 2014;47:414–20.
47. Jubb AM, Allen HC. Vibrational spectroscopic characterization of hematite, maghemite, and magnetite thin films produced by vapor deposition. *ACS Appl Mater Interfaces.* 2010;2(10):2804–12.
48. Voigt B, Göbner A. Formation of pure haematite by hydrolysis of iron(III) salt solutions under hydrothermal conditions. *Cryst Res Technol.* 1986;21(9):1177–83.
49. Rosebrock CD, Riefner N, Wriedt T, Mädler L, Tse SD. Disruptive burning of precursor/solvent droplets in flame-spray synthesis of nanoparticles. *AIChE J.* 2013;59(12):4553–66.
50. Harra J, Kujanpää S, Haapanen J, Juuti P, Mäkelä JM. Aerosol analysis of residual and nanoparticle fractions from spray pyrolysis of poorly volatile precursors. *AIChE J.* 2017;63(3):881–92.
51. Rosebrock CD, Wriedt T, Mädler L, Wegner K. The role of micro-explosions in flame spray synthesis for homogeneous nanopowders from low-cost metal precursors. *AIChE J.* 2016;62(2):381–91.
52. Chiarello GL, Rossetti I, Forni L, Lopinto P, Migliavacca G. Solvent nature effect in preparation of perovskites by flame pyrolysis 2.

- Alcohols and alcohols + propionic acid mixtures. *Appl Catal B Environ.* 2007;72:227–32.
53. Habibi MH, Kiani N. Preparation of single-phase α -Fe(III) oxide nanoparticles by thermal decomposition. Influence of the precursor properties. *J Therm Anal Calorim.* 2013;112:573–7.
 54. Meierhofer F, Li H, Gockeln M, Kun R, Grieb T, Rosenauer A, et al. Screening precursor-solvent combinations for $\text{Li}_4\text{Ti}_5\text{O}_{12}$ energy storage material using flame spray pyrolysis. *ACS Appl Mater Interfaces.* 2017;9:37760–77.
 55. Grigorie AC, Muntean C, Stefanescu M. Obtaining of γ - Fe_2O_3 nanoparticles by thermal decomposition of polyethyleneglycol-iron nitrate mixtures. *Thermochim Acta.* 2015;621:61–7.

SUPPORTING INFORMATION

Additional supporting information may be found online in the Supporting Information section at the end of the article.

How to cite this article: Sorvali M, Nikka M, Juuti P, et al. Controlling the phase of iron oxide nanoparticles fabricated from iron(III) nitrate by liquid flame spray. *Int J Ceramic Eng Sci.* 2019;1:194–205. <https://doi.org/10.1002/ces2.10025>